## High performance, room temperature, broadband II-VI quantum cascade detector

Cite as: Appl. Phys. Lett. **107**, 141105 (2015); https://doi.org/10.1063/1.4932538 Submitted: 29 July 2015 . Accepted: 20 September 2015 . Published Online: 05 October 2015

Arvind P. Ravikumar 🗓, Joel De Jesus, Maria C. Tamargo, and Claire F. Gmachl







## ARTICLES YOU MAY BE INTERESTED IN

InAs/AlAsSb based quantum cascade detector

Applied Physics Letters 107, 081107 (2015); https://doi.org/10.1063/1.4929501

High photoresponse in room temperature quantum cascade detector based on coupled quantum well design

Applied Physics Letters 109, 261107 (2016); https://doi.org/10.1063/1.4973582

The limit of quantum cascade detectors: A single period device Applied Physics Letters 111, 061107 (2017); https://doi.org/10.1063/1.4985711







## High performance, room temperature, broadband II-VI quantum cascade detector

Arvind P. Ravikumar, 1,a) Joel De Jesus, Maria C. Tamargo, and Claire F. Gmachl

<sup>1</sup>Department of Electrical Engineering, Princeton University, Princeton, New Jersey 08544, USA

(Received 29 July 2015; accepted 20 September 2015; published online 5 October 2015)

We report on the experimental demonstration of a room temperature, II-VI, ZnCdSe/ZnCdMgSe, broadband Quantum Cascade detector. The detector consists of 30 periods of 2 interleaved activeabsorption regions centered at wavelengths 4.8  $\mu$ m and 5.8  $\mu$ m, respectively. A broad and smooth photocurrent spectrum between 3.3  $\mu$ m and 6  $\mu$ m spanning a width of 1030 cm<sup>-1</sup> measured at 10% above baseline was obtained up to 280 K, corresponding to a  $\Delta E/E$  of 47%. Calibrated blackbody responsivity measurements show a measured peak responsivity of 40 mA/W at 80 K, corresponding to a detectivity of about  $3.1 \times 10^{10} \,\mathrm{cm}\sqrt{\mathrm{Hz}}/\mathrm{W}$ . Bias dependent photocurrent measurements revealed no significant change in the spectral shape, suggesting an impedance matched structure between the different active regions. © 2015 AIP Publishing LLC.

[http://dx.doi.org/10.1063/1.4932538]

Broadband infrared detectors are useful in various applications, the most important and extensive of which are in making infrared cameras used in military applications, astronomical observations, and spectroscopy. Existing solutions like HgCdTe detectors offer high sensitivity only at cryogenic temperatures, and cannot be used in high-speed applications such as heterodyne spectroscopy. In this context, intersubband (ISB) infrared detectors like Quantum Well Infrared Photodetectors (QWIPs)<sup>1</sup> and Quantum Cascade Detectors (QCDs)<sup>2</sup> have become attractive options to develop sensitive, high-speed, and portable detectors. Because these intersubband detectors are not limited by material bandgap, they can be used to demonstrate spectrally broadband detection. Historically made from lattice-matched GaAs/AlGaAs system, initial attempts at developing broadband QWIPs<sup>3-7</sup> were restricted to the long-wavelength regime. In order to extend wavelength coverage and improve performance, other materials like strain-balanced InGaAs/InAlAs system,8 nitride-based system, <sup>9</sup> Sb-based materials, <sup>10</sup> and more recently, quantumdot devices<sup>11</sup> have been explored. While functional, in principle, many of these materials suffer from issues like carrier scattering into satellite valleys, size non-uniformity of quantum dots, or internal fields that complicate design.

On a similar note, broadband detectors have been made from different materials including InGaAs/InGaAsP, <sup>12</sup> strained Si/Si-Ge, 13 or SiGe quantum dots. 14 Broadband detection in the mid-wave infrared (5–8  $\mu$ m) was demonstrated using QCDs, 15 achieving a peak responsivity of 13 mA/W at 10 K, by stacking 26 different active stage designs. More recently, 16 a QCD operating in two spectral bands was demonstrated. QCDs have superior noise properties compared to QWIPs owing to their operation at zero bias, and are therefore suitable for high sensitivity applications.

The II-VI ZnCdSe/ZnCdMgSe material system is well suited to develop broadband infrared detectors from the near-IR to long-wave IR because of the large conduction band offset of up to 1.1 eV, <sup>17</sup> and the absence of satellite valleys near the  $\Gamma$  point of the conduction band of the well. 18 Previously, we have demonstrated long-wave QWIPs, <sup>19</sup> roomtemperature short-wave QWIPs,<sup>20</sup> and a high-detectivity II-VI based Quantum Cascade detector<sup>21</sup> using this material system. In this paper, we demonstrate what could arguably be called the poster-child for the capability of II-VI materials—a room temperature, broadband QCD. We use a two interleaved active-absorber regions to achieve a spectral width of over 1000 cm<sup>-1</sup>, a peak responsivity of 40 mA/W, and a background limited detectivity of over  $10^{10} \text{ cm} \sqrt{\text{Hz}}/\text{W}$  at 80 K.

The energy states and wavefunctions of the detector were calculated within a one-band conduction band model with an energy dependent effective mass that accounts for band mixing and non-parabolicity effects.<sup>22</sup> The broadband detector consisted of two interleaved active absorber regions, each with center wavelengths at 4.8  $\mu$ m and 5.8  $\mu$ m, respectively. Figure 1(a) shows the conduction band diagram of the long wavelength absorber, with a transition energy centered at 212 meV. The upper detection level consists of three coupled states with transition energies 204 meV, 212 meV, and 223 meV. Similarly, the transition energies of the three coupled upper detection states of the short-wave core (see Figure 1(b)) are 240 meV, 252 meV, and 267 meV. The main detection well in each of the two active absorbers is Chlorine doped to  $1 \times 10^{18} \, \text{cm}^{-3}$ . The states in the extractor region are separated by about one longitudinal optical phonon in energy (about 35 meV in II-VI materials) to facilitate fast carrier relaxation towards the next period. For the remainder of this paper, a period of this detector will be defined as the sum of the periods of the two individual active absorber regions, corresponding to a total length of 74.7 nm. Thirty periods consisting of Zn<sub>0.51</sub>Cd<sub>0.49</sub>Se wells and Zn<sub>0.29</sub>Cd<sub>0.26</sub>Mg<sub>0.45</sub>Se barriers

<sup>&</sup>lt;sup>2</sup>Department of Physics, The Graduate Center and The City College of New York, CUNY, New York, New York 10031, USA

<sup>&</sup>lt;sup>3</sup>Department of Chemistry, The Graduate Center and The City College of New York, CUNY, New York, New York 10031, USA

a)aravikum@princeton.edu

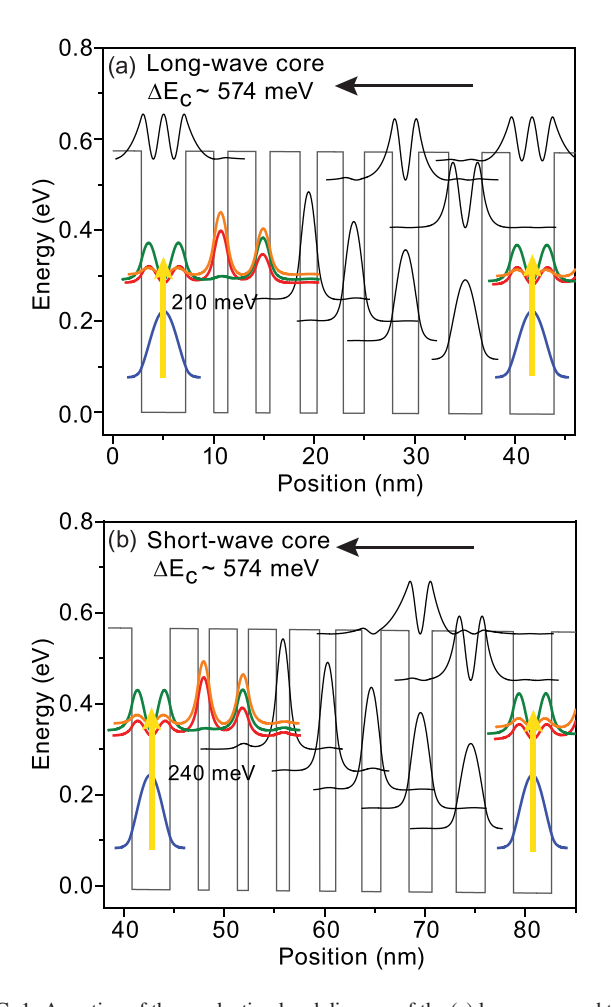


FIG. 1. A portion of the conduction band diagram of the (a) long-wave and the (b) short-wave absorber regions of the broadband detector. The layer thicknesses (in Angstroms), starting from the main detection well for the long-wave core, are as follows:  $\underline{44}/28/14/28/14/30/17/26/21/28/26/30/33/28$ , where the  $Z_{00.51}Cd_{0.49}Se$  wells are given in normal font while the  $Z_{00.29}Cd_{0.26}Mg_{0.45}Se$  barriers are in bold font. The underlined layers are doped to  $1\times10^{18}~cm^{-3}$ . The layers thicknesses of the short-wave core are as follows:  $\underline{38}/28/11/28/11/28/13/30/16/26/19/28/23/24/29/28$ . Forward bias in these QCDs is indicated by an arrow.

were grown using Molecular Beam Epitaxy (MBE) on a semi-insulating InP substrate. The active core was sandwiched between highly doped (Cl:  $1 \times 10^{18} \, \text{cm}^{-3}$ ) top (100 nm) and bottom (800 nm) contact layers. X-Ray diffraction measurements showed sharp satellite peaks indicating good growth quality, and a measured period of 71.2 nm, corresponding to a 5% reduction in the layer thicknesses. Photoluminescence measurements on a single ZnCdMgSe barrier layer grown immediately after the detectors indicated a barrier material bandgap of 2.92 eV at 300 K, higher than the 2.8 eV used in calculations corresponding to a higher Mg content in the quaternary layers. The combined result of these two deviations will result in the detection wavelength to be blue shifted compared to designed values. These wafers were then processed into rectangular mesas,  $310 \, \mu \text{m} \times 485 \, \mu \text{m}$  using standard optical lithography and wet chemical etching methods. Top and bottom contacts of Ti (20 nm)/Au (200 nm) were deposited by electron beam evaporation. The top of the mesa has an opening  $300 \,\mu\text{m} \times 300 \,\mu\text{m}$  for optical measurements.

Figure 2(a) shows the dark current-voltage (I-V) characteristics of the device as a function of temperature. At an applied bias of 500 mV, the dark current density increases

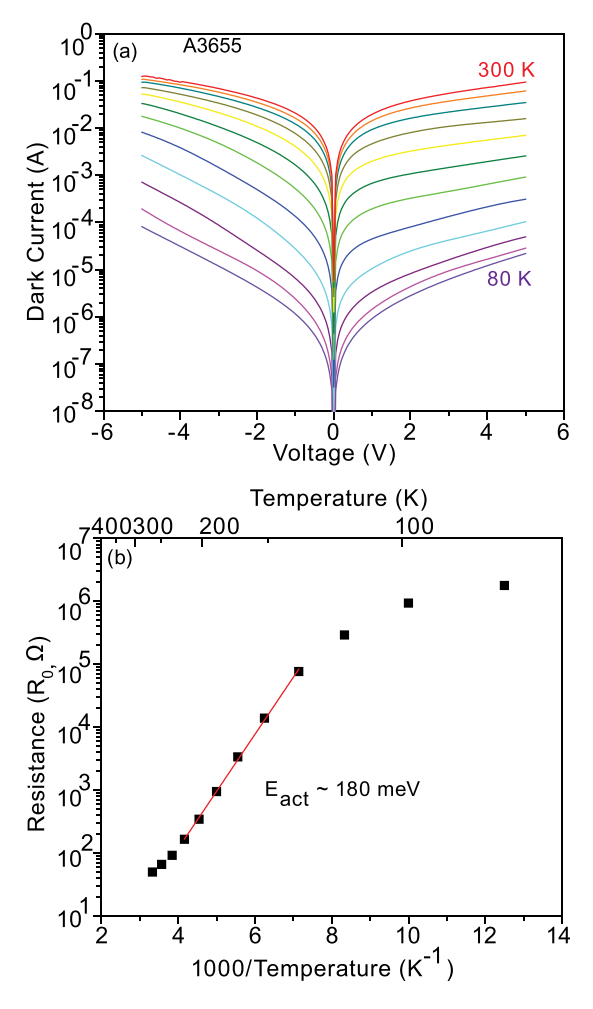


FIG. 2. (a) Temperature dependent dark current-voltage (I-V) measurements of the detector. The device differential resistance ( $R_0$ ), whose square-root is directly proportional to the Johnson noise current, decreases from about 1.8 M $\Omega$  at 80 K to 50  $\Omega$  at 300 K. Positive fields (negative voltages) corresponds to forward biasing the detector. (b) Arrhenius plot of the device dark current, showing an effective activation energy of 180 meV.

from about  $2.4\,\text{mA/cm}^2$  at  $80\,\text{K}$  to about  $6.7\,\text{A/cm}^2$  at  $300\,\text{K}$ . The asymmetric nature of the I-V is consistent with the band structure of the detector. The product of the area of the device (A) and its differential resistance at  $0\,\text{V}$  bias (R<sub>0</sub>) is indicative of the Johnson noise in the detector. An Arrhenius plot of the device differential resistance is shown in Figure 2(b). The R<sub>0</sub>A product of this detector decreases from about  $2.7\,\text{k}\Omega\,\text{cm}^2$  at  $80\,\text{K}$  to about  $0.075\,\Omega\,\text{cm}^2$  at  $300\,\text{K}$ , corresponding to an activation energy of  $180\,\text{meV}$ . Given the broadband nature of the transition, this value of activation energy can be interpreted as an average thermal energy required for conduction under dark conditions.

Figures 3(a) and 3(b) summarize the spectral characteristics of the broadband detector. These measurements were taken using a Fourier Transform Infrared Spectrometer (FTIR) with the device at 45° to incoming radiation. It should be noted that the spectral measurements up to 220 K were obtained in the fast-scan mode of the FTIR. For spectra beyond 220 K, the FTIR light source is sampled using a mechanical chopper at 279 Hz, and the amplified photocurrent is detected using standard lock-in techniques. No significant difference was found in the spectral characteristics measured using the two methods. The detector has a broad as well as smooth spectral response

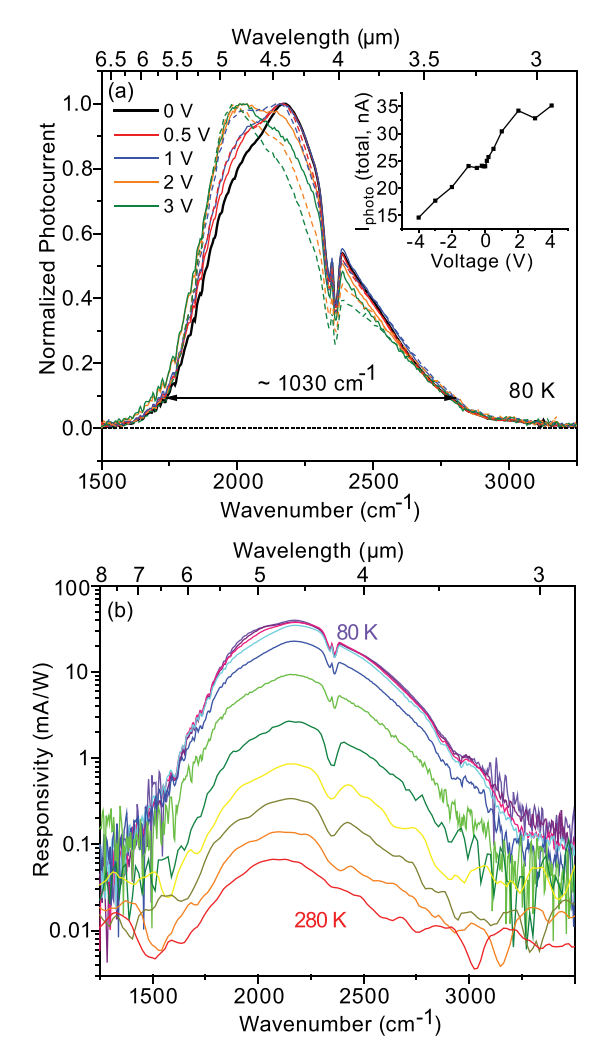


FIG. 3. (a) Bias dependent normalized spectral photocurrent characteristics of the broadband detector at 80 K taken using an FTIR. A smooth and broad spectrum was obtained between 3.3  $\mu m$  and 6  $\mu m$ , with a spectral width of  $1030\, {\rm cm}^{-1}$  measured at 10% above baseline, corresponding to a  $\Delta E/E$  of 47%. A slight red shift in the peak wavenumber can be seen as bias increases from 0 V through 3 V. This is the result of some impedance mismatch between the two active absorbers. (Inset) Absolute integrated photocurrent as a function of applied bias. Due to the asymmetric nature of the bandstructure, we see a monotonic increase in responsivity with increasing bias. (b) Temperature dependent photocurrent spectrum at zero bias plotted on a log-scale. The broad spectral response seen at 80 K with a width 1030 cm $^{-1}$  was obtained through 280 K. A peak responsivity of 40 mA/W was obtained at 80 K.

between 3.3  $\mu$ m and 6  $\mu$ m, as shown in Figure 3(a), taken at 80 K at different applied bias voltages. At zero bias, we measure a spectral width of 1030 cm<sup>-1</sup>, measured at 10% above baseline (shown by a dotted black line), corresponding to 47% of the peak wavenumber at 2175 cm<sup>-1</sup>. As explained previously, the spectral peaks of the detector is blue-shifted from  $1710\,\mathrm{cm}^{-1}$  (212 meV) to  $1935\,\mathrm{cm}^{-1}$  (240 meV) for the longwave absorber, and from  $2030\,\mathrm{cm}^{-1}$  (252 meV) to  $1935\,\mathrm{cm}^{-1}$ (291 meV) for the short-wave absorber. With increasing applied bias (both forward and reverse), the energy difference between the two absorber states decreases, resulting in a redshifted spectrum. Concurrently, we also see a smooth transition in the peak of the spectrum with increasing bias—the peak is at 4.4  $\mu$ m at zero bias, becoming a double-peak around  $\pm 1 \,\mathrm{V}$ and finally to around 4.8  $\mu$ m at  $\pm 3$  V. This transition is typically seen in broadband detectors, arising mainly from the impedance mismatch between the two absorber regions resulting in unequal voltage drops. At small applied bias, much of the applied bias drops across the short-wave core (higher impedance). As the bias increases, the voltage drop across the long-wave absorber increases, and hence, long wave absorption becomes prominent. In terms of absolute magnitude of the photocurrent, the asymmetric nature of the bandstructure affects the extraction efficiency for forward and reverse bias, resulting in a monotonic change in photocurrent. This is shown in the inset of Figure 3(a)—the integrated photocurrent linearly increases from 24 nA at zero bias to 35 nA at a forward bias of  $+4 \,\mathrm{V}$ , and decreases to 14.6 nA at a reverse bias of  $-4 \,\mathrm{V}$ . Figure 3(b) shows the temperature dependent spectral characteristics of the detector at zero bias. It can be noted that the smoothness and width of the spectral response is maintained up to room temperature. In addition, we also measured a peak responsivity of 40 mA/W at 80 K—this is the highest reported responsivity for any QC detector around 4  $\mu$ m at this temperature. Responsivity measurements are discussed in the next paragraph. With this, we also show that it is possible to simultaneously achieve a broad spectral response (over 1000 cm<sup>-1</sup>) and a high peak responsivity (40 mA/W).

In order to measure absolute responsivity, we use a calibrated blackbody source at 900 °C, with the detector at a distance D of 18 cm from the blackbody with an aperture of diameter a, 1 in. Integrated photocurrent is measured with a chopper running at 279 Hz, connected to a trans-impedance amplifier at 100 nA/V sensitivity, and detected using a standard lock-in amplifier. This integrated photocurrent,  $I_{total}$ , can be written as

$$I_{total} = \frac{1}{2} R_p \int_{-\infty}^{+\infty} \tilde{R}(\lambda) P(\lambda) d\lambda, \tag{1}$$

where  $P(\lambda)$ , the spectral power incident on the detector is given by

$$P(\lambda) = W(\lambda) \operatorname{Sin}^{2} \left(\frac{\Omega}{2}\right) A C_{F} \operatorname{Cos}(\theta). \tag{2}$$

 $R_p$  is the peak responsivity at wavelength  $\lambda_p$ ,  $\tilde{R}(\lambda)$  is the normalized photocurrent spectrum,  $W(\lambda)$  is the blackbody spectral density given by Planck's radiation law,  $\Omega$  is the optical field of view angle of the detector such that,  $\tan(\Omega/2) = a/D$ , A is the detector cross-section area,  $C_F$  is the coupling factor, and  $\theta$  is the angle of incidence. The coupling factor  $C_F$  consists of three terms, given by,  $C_F = T_f(1-r)C^*$ ;  $T_f$  is the transmission of various filters and windows used in the beam path, r is the reflectivity of the ZnCdSe detector surface calculated using Fresnel's equations for an effective refractive index of 2.3, and  $C^*$  is the optical chopper factor. For an ideal chopper, this value is exactly 0.5, corresponding to the duty cycle. In our experiments, we calculate a chopper factor of 0.32. Detailed calculations for the chopper factor can be found elsewhere.  $^{23}$ 

Using the method mentioned above, we measured the responsivity of the detector at zero bias as a function of temperature as shown in Figure 4(a). Aside from a peak responsivity of 40 mA/W at 80 K, we notice that the value drops

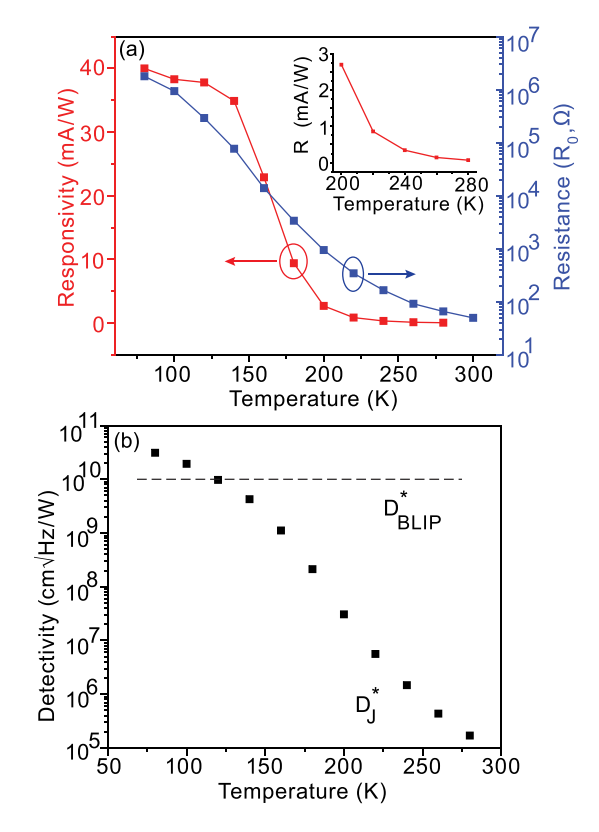


FIG. 4. (a) Temperature dependent peak responsivity (red, left axis) and device differential resistance (blue, right axis). We obtain a peak responsivity of 40 mA/W at 80 K, which rapidly decreases above the background limited infrared performance (BLIP) temperature of 120 K. Concurrently, the device differential resistance also reduces from over 1 M $\Omega$  at 80 K to about 50  $\Omega$  at 280 K. (Inset) An expanded view of the responsivity from 200 K to 280 K. (b) Peak detectivity of the detector as a function of temperature. The black horizontal line denotes background limited performance—we obtain a peak background limited detectivity of about  $10^{10} \text{ cm} \sqrt{\text{Hz}}/\text{W}$  at 120 K.

slowly until about 120 K, and then falls sharply beyond that due to increased phonon scattering. The device can achieve background limited performance up to 120 K. Beyond 120 K, Johnson noise in the detector plays a dominant role and degrades performance. The device differential resistance at zero bias,  $R_0$ , indicative of the Johnson noise in the detector, is also plotted as a reference. The detectivity of the device, a measure of its sensitivity, is shown in Figure 4(b). We achieve a high peak detectivity of  $3.1 \times 10^{10} \, \text{cm} \sqrt{\text{Hz}}/\text{W}$  at 80 K, with a background limited detectivity of approximately  $10^{10} \,\mathrm{cm} \sqrt{\mathrm{Hz}} / \mathrm{W}$  at  $120 \,\mathrm{K}$  (shown by the black horizontal line). Beyond that, the Johnson noise limited detectivity rapidly decreases to just over  $10^5 \,\mathrm{cm}\sqrt{\mathrm{Hz}}/\mathrm{W}$  at 280 K. This number, while low, can be easily improved by adopting various optical coupling techniques.

In summary, we have developed a high performance, II-VI ZnCdSe/ZnCdMgSe based broadband QCD. The detector core consists of 30 periods of interleaved dualabsorber active region design, with peak detection wavelength of each absorber centered at 4.8  $\mu$ m and 5.8  $\mu$ m, respectively. A smooth and broad spectral response between  $3.3 \,\mu\mathrm{m}$  and  $6 \,\mu\mathrm{m}$  was obtained up to  $280 \,\mathrm{K}$ , with a spectral width of 1030 cm<sup>-1</sup> at 10% above baseline, corresponding to a  $\Delta E/E$  of 47%. Blackbody measurements show a peak responsivity of 40 mA/W at 80 K, corresponding to a detectivity of  $3.1 \times 10^{10} \,\mathrm{cm}\sqrt{\mathrm{Hz}}/\mathrm{W}$ . Background limited performance is achieved up to 120 K, with a limiting detectivity of about  $10^{10} \, \text{cm} \sqrt{\text{Hz}}/\text{W}$ . This detector demonstrates that one can obtain broad spectral response as well as a high peak responsivity in intersubband IR detectors.

We acknowledge funding from the National Science Foundation through the MIRTHE (EEC-0540832), AIR-TT (IIP-1414266), and the CENSES award.

<sup>1</sup>B. Levine, J. Appl. Phys. **74**, R1 (1993).

<sup>2</sup>F. R. Giorgetta, E. Baumann, M. Graf, Q. Yang, C. Manz, K. Köhler, H. E. Beere, D. Ritchie, E. Linfield, A. G. Davies et al., IEEE J. Quantum Electron. 45, 1039 (2009).

<sup>3</sup>B. Levine, G. Hasnain, C. Bethea, and N. Chand, Appl. Phys. Lett. 54, 2704 (1989).

<sup>4</sup>S. Bandara, S. Gunapala, J. Liu, E. Luong, J. Mumolo, W. Hong, D. Sengupta, and M. McKelvey, Appl. Phys. Lett. 72, 2427 (1998).

<sup>5</sup>A. Ellis, A. Majumdar, K. Choi, J. Reno, and D. Tsui, Appl. Phys. Lett. 84, 5127 (2004).

<sup>6</sup>S. Bandara, S. Gunapala, J. Liu, S. Rafol, C. Hill, D.-Y. Ting, J. Mumolo, T. Trinh, J. Fastenau, and A. Liu, Appl. Phys. Lett. 86, 151104 (2005).

<sup>7</sup>H. Liu, D. Goodchild, M. Byloos, M. Buchanan, Z. Wasilewski, J. Gupta, A. SpringThorpe, and G. Aers, Infrared Phys. Technol. 50, 171 (2007).

<sup>8</sup>F. Giorgetta, E. Baumann, R. Theron, M. Pellaton, D. Hofstetter, M. Fischer, and J. Faist, Appl. Phys. Lett. 92, 121101 (2008).

<sup>9</sup>A. Vardi, N. Kheirodin, L. Nevou, H. Machhadani, L. Vivien, P. Crozat, M. Tchernycheva, R. Colombelli, F. Julien, F. Guillot, C. Bougerol, E. Monroy, S. Schacham, and G. Bahir, Appl. Phys. Lett. 93, 193509 (2008).

<sup>10</sup>F. R. Giorgetta, E. Baumann, D. Hofstetter, C. Manz, Q. Yang, K. Kohler, and M. Graf, Appl. Phys. Lett. 91, 111115 (2007).

<sup>11</sup>A. Barve and S. Krishna, Appl. Phys. Lett. **100**, 021105 (2012).

<sup>12</sup>J. Li, K. Choi, J. Klem, J. Reno, and D. Tsui, Appl. Phys. Lett. 89, 081128

<sup>13</sup>R. People, J. Bean, C. Bethea, S. Sputz, and L. Peticolas, Appl. Phys. Lett. 61, 1122 (1992).

<sup>14</sup>C.-H. Lin, C.-Y. Yu, C.-Y. Peng, W. Ho, and C. Liu, J. Appl. Phys. 101, 033117 (2007).

<sup>15</sup>D. Hofstetter, F. R. Giorgetta, E. Baumann, Q. Yang, C. Manz, and K. Köhler, Appl. Phys. Lett. 93, 221106 (2008).

<sup>16</sup>P. Reininger, B. Schwarz, H. Detz, D. MacFarland, T. Zederbauer, A. M. Andrews, W. Schrenk, O. Baumgartner, H. Kosina, and G. Strasser, Appl. Phys. Lett. **105**, 091108 (2014).

<sup>17</sup>M. Sohel, X. Zhou, H. Lu, M. N. Perez-Paz, M. Tamargo, and M. Muñoz, J. Vac. Sci. Technol. B 23, 1209 (2005).

<sup>18</sup>O. Zakharov, A. Rubio, X. Blase, M. L. Cohen, and S. G. Louie, Phys. Rev. B 50, 10780 (1994).

<sup>19</sup>A. P. Ravikumar, A. Alfaro-Martinez, G. Chen, K. Zhao, M. C. Tamargo, C. F. Gmachl, and A. Shen, Opt. Express 20, 22391 (2012).

<sup>20</sup>A. P. Ravikumar, G. Chen, K. Zhao, Y. Tian, P. Prucnal, M. C. Tamargo, C. F. Gmachl, and A. Shen, Appl. Phys. Lett. 102, 161107 (2013).

<sup>21</sup>A. P. Ravikumar, T. A. Garcia, J. De Jesus, M. C. Tamargo, and C. F. Gmachl, Appl. Phys. Lett. 105, 061113 (2014).

<sup>22</sup>C. Sirtori, F. Capasso, J. Faist, and S. Scandolo, Phys. Rev. B 50, 8663

<sup>23</sup>R. B. McQuistan, J. Opt. Soc. Am. 49, 70 (1959).